Pathological tau disrupts ongoing network activity

Pathological tau disrupts ongoing network activity

Noa Menkes-Caspi[1], Hagar G. Yamin[1], Vered Kellner[1], Tara L. Spires-Jones[2], Dana Cohen[1], and Edward A. Stern[1,3]

[1] Gonda Brain Research Center, Bar-Ilan University, Ramat Gan, Israel

[2] Centre for Cognitive and Neural Systems and Euan MacDonald Centre for Motorneurone Disease Research, University of Edinburgh, Edinburgh, UK

[3] MassGeneral Institute for Neurodegenerative Disease, Dept. Of Neurology, Massachusetts General Hospital, Charlestown, MA, USA

All correspondence should be addressed to:

Edward A. Stern

Gonda Brain Research Center

Bar-Ilan University

Ramat Gan 52900 Israel

Tel: +972-3-531-7367

Email:sterned@mail.biu.ac.il

SUMMARY

Pathological tau is a key factor leading to dementia and neurodegeneration in tauopathies, including Alzheimer's Disease. Pathological tau has been shown to disrupt cellular and synaptic functions, yet its effects on the physiological function of the intact neocortical network remain unknown. Using intracellular and extracellular *in vivo* recordings, we measured ongoing activity of neocortical pyramidal cells during various arousal states in the rTg4510 mouse model of tauopathy. We found that in anesthetized mice the characteristic patterns of ongoing subthreshold membrane potential dynamics, which result from synaptic input patterns, are altered in transgenic neurons, as are their firing patterns. We found a similar change in oscillation patterns and firing rates in freely behaving transgenic mice during slow wave sleep. These changes occur at a pathological stage prior to significant neurodegeneration. By changing the activity patterns of a subpopulation of affected neurons, pathological tau disrupts the activity patterns of the neocortical network.

RUNNING TITLE

Pathological tau disrupts ongoing network activity

HIGHLIGHTS

- Pathological tau disrupts the activity of single cells and neocortical networks.
- Pathological tau alters neocortical neuronal oscillatory patterns.
- Pathological tau affects firing patterns of neocortical pyramidal cells.

INTRODUCTION

Tau is a microtubule-associated protein which binds and stabilizes neuronal microtubules, primarily in axons. In tauopathies, neurodegenerative diseases characterized by dementia, including Alzheimer's Disease, tau is hyperphosphorylated and aggregates into neurofibrillary tangles (NFTs) in an age-dependent manner (reviewed in Avila et al., 2004; Gendron and Petrucelli, 2009). Pathological tau causes morphological changes in neurites (Crimins et al., 2012; Crimins et al., 2011; Knowles et al., 1999; Rocher et al., 2009; Stokin et al., 2005) and synapses (DeKosky and Scheff, 1990; Kopeikina et al., 2013; Thies and Mandelkow, 2007; Yoshiyama et al., 2007), and impairs cellular trafficking (Kopeikina et al., 2011; Roy et al., 2005; Shemesh et al., 2008; Stamer et al., 2002; Stokin et al., 2005; Thies and Mandelkow, 2007) and synaptic function (Hoover et al., 2010; Moreno et al., 2011; Yoshiyama et al., 2007). In the rTg4510 model, a well-characterized model of tauopathy, mice overexpress human mutant P301L tau in forebrain structures. These mice display progressive cognitive decline and subsequent cell death concomitant with tau accumulation (Santacruz et al., 2005; Spires et al., 2006). Cognitive deficits are initially observed at a stage in which pathological tau affects a fraction of the neurons, prior to substantial neurodegeneration (Hoover et al., 2010; Ramsden et al., 2005; Santacruz et al., 2005). However, most studies in the rTg4510 line are conducted in mice at a later pathological stage; in many cases, following substantial cell death in several forebrain regions. At earlier stages of the disease, up to 5.5 months of age, no distinct changes to spine or synaptic density or structure are observed in rTg4510 transgenic mice (Crimins et al., 2012; Hoover et al., 2010; Kopeikina et al., 2013). Electrophysiological studies in rTg4510 transgenic mice have mostly been performed in animals over 7 months old, following substantial neuronal death. These studies

have shown altered firing patterns of hippocampal neurons (Cheng and Ji, 2013), and suggested hyperexcitability of neocortical neurons recorded *in vitro* (Crimins et al., 2012; Crimins et al., 2011; Rocher et al., 2009). However, the effects of pathological tau on the functional activity of the intact neocortical network, possibly underlying cognitive decline in tauopathies, are still unclear.

In the intact neocortical network, the membrane potentials of pyramidal neurons show characteristic patterns of spontaneous ongoing activity, which are not present in acute reduced preparations. During slow-wave sleep (SWS) and under ketamine-xylazine (KX) anesthesia, the membrane potential spontaneously transitions between the hyperpolarized silent Down state (resting membrane potential) and the depolarized Up state, from which action potentials (APs or spikes) arise, with a dominant oscillatory frequency of ~1 Hz (Cowan and Wilson, 1994; Steriade et al., 1993). The Up states are generated by a barrage of synchronous convergent synaptic inputs, occasionally inducing the cell to spontaneously fire, and when ceased, cause the membrane potential to fall into the Down state (Haider et al., 2006; Leger et al., 2005). KX anesthesia serves as a model for SWS, as both show slow rhythmic, stereotypical fluctuations of the membrane potential in the subthreshold range, which are also seen in the field potential recordings, and reflect high synchronization. However, fine differences exist between these two states. Under anesthesia, a stronger rhythmicity of slow oscillation was observed in field potential and intracellular recordings of cats, as well as longer durations of Down states (Chauvette et al., 2011). The ongoing background activity of the neuron shapes the responses of the neuron to evoked inputs (Arieli et al., 1996; Bernander et al., 1991; Leger et al., 2005; Stern et al., 1997).

In this study, we measured the effects of mutant tau overexpression on the function of the intact neocortical network using *in vivo* intracellular and extracellular recordings of spontaneous ongoing activity from frontal pole (medial and lateral agranular cortex) pyramidal neurons in rTg4510 tau-transgenic mice (Tg) and their age-matched non-transgenic littermates (Ctrl or controls). We used intracellular recordings from neurons in anesthetized animals to measure changes to subthreshold membrane potential dynamics and spiking, and extracellular recordings in freely-moving animals to measure single cell and multicellular activity during SWS and quiet wakefulness (QW). Changes in the overall pattern of spontaneous subthreshold membrane potential fluctuations of single neurons reveal changes in the envelope of activity of the cortical network of afferents, as these states are induced by periods of intense (Up state) and sparse (Down state) background network activity (Haider et al., 2006; Leger et al., 2005). Chronic extracellular *in vivo* recordings in freely behaving transgenic mice and their age-matched controls further elucidate the effects of pathological tau on the function of the nonanesthetized intact neocortical network during SWS and QW.

RESULTS

Ongoing activity was measured using *in vivo* intracellular and extracellular recordings in separate experiments. We recorded intracellularly from 63 frontal pole neurons in 39 anesthetized rTg4510 transgenic and control mice. Recordings were made in two age cohorts: 3-3.5 months old mice ("3mo") and 4.5-6 months old mice ("5mo"), displaying moderate NFT accumulation in the neocortex prior to appreciable cell death (Figure S1; see Supplemental Experimental Procedures), with the latter group showing variable yet significantly higher levels of NFT accumulation ($p = 0.02$, t-test). This is in agreement with a previous study showing significant NFT

accumulation in rTg4510 cortex starting at 2.5 months of age, but no significant cortical neuronal loss until 8.5 months (Spires et al., 2006). Intracellular recordings were conducted in neocortical pyramidal neurons identified by physiological characteristics (Connors and Gutnick, 1990; Connors et al., 1982; McCormick et al., 1985) and, when possible, histologically (Figure 1A). Spontaneous membrane potential fluctuations between Up and Down states were observed in all intracellularly recorded neurons (Figures 1B and 1C). No differences among the membrane potential or input resistance values were observed between groups (Table S1), indicating that passive electrical properties of these cells are not altered by pathological tau.

We recorded local field potentials (LFPs) during QW and SWS from four 5mo transgenic mice and seven 5mo controls in 10 and 16 experiments, respectively. Extracellular single-unit recordings were performed during QW and SWS on a subset of three 5mo transgenic mice and three 5mo controls, yielding 27 units from each group. For these experiments, microwire electrode arrays were implanted in the frontal pole of the cortex extending 2 mm rostrocaudally and 1 mm mediolaterally to bregma. The location of the electrode tips was verified histologically (Figure 1D; see Experimental Procedures). Single unit recordings of neocortical pyramidal neurons from both groups were identified by waveform parameters (Bartho et al., 2004; Figures 1E and 1F). Mice from both groups showed LFP recordings typical of QW and SWS epochs (Gervasoni et al., 2004; Figures 1E, 1F and S2).

** Figure 1 about here **

Differences in patterns of subthreshold membrane potential oscillations between neurons in transgenic mice and controls can reveal altered activity of the pathological-tau-burdened neocortical network. To quantify these changes, we compared the mean

oscillatory period of the membrane potential fluctuations (i.e. the duration between successive transitions to Up states) in our intracellular recordings among groups. Neurons in 5mo transgenic mice had longer periods than controls (Figures 2A and 3C; $p \approx 0$, K-sample Anderson-Darling test; $p_{genotype} = 0.0006$, Genotype × Age ANOVA and $p < 0.05$, Tukey post-hoc test). Spectral analysis of the subthreshold activity revealed all groups to have a principal frequency (i.e. frequency at maximum power) in the slow oscillation range (<1 Hz). However, neurons in 5mo transgenic mice had a lower principal frequency than controls (Figure 2B; $p_{genotype} = 0.012$, Genotype × Age ANOVA and $p < 0.05$, Tukey post-hoc test), in accordance with their slower membrane potential dynamics. For a more direct measure of the changes in neocortical network function, we compared the frequency composition of LFP recordings between 5mo transgenic mice and their age-matched controls during QW and SWS. Spectral analysis revealed the principal frequency of individual LFPs in control mice to be either in the delta (1-4 Hz) or the spindle (7-14 Hz) frequency ranges, while the principal frequency of individual LFPs in transgenic mice was always in the delta range. In order to quantify the observed power spectrum differences in the spindle frequency range (7-14 Hz) and the delta range (1-4 Hz), we calculated the spindle-delta power ratio of the LFP recordings (see Experimental Procedures). During both QW and SWS 5mo transgenic mice had a reduced spindle-delta power ratio compared with that of controls (Figure 2C; QW: $p = 0.02$, SWS: $p = 0.008$, t-test). All groups had an average principal frequency in the delta frequency range during both behavioral states (Figure 2C). During SWS, 5mo transgenic mice had a lower principal frequency than controls ($p = 0.03$, t-test), while during QW no difference was observed (Figure 2C; $p = 0.15$, t-test). Taken together, these findings

suggest that pathological tau perturbs highly synchronous epochs of activity, such as SWS and under anesthesia.

To identify the affected components of the membrane potential periodicity, we measured the individual durations of membrane potential states and their transitions during intracellular recordings. No differences were found for average Up state durations (data not shown; $p_{genotype} = 0.098$, Genotype × Age ANOVA). However, Down state durations of neurons in transgenic mice were longer than those in controls (Figure 2D; $p = 0.02$, K-sample Anderson-Darling test; $p_{genotype} = 0.0009$, Genotype × Age ANOVA and $p < 0.05$, Tukey post-hoc test). The within-cell variability of Down state durations of neurons in 5mo transgenic mice was greater than in controls (Figure 2D; $p_{genotype} = 0.0034$, Genotype × Age ANOVA and $p < 0.05$, Tukey post-hoc test). The longer Down state durations could arise from an effect of pathological tau on the postsynaptic neuron, such as increasing the inward-rectifying potassium conductance, and/or from an insufficient number and/or synchrony of synaptic inputs to cause a voltage shift to the Up state in the postsynaptic membrane. The greater within-cell variability of Down state durations also suggests a reduction in sufficient synchronous synaptic input, as neuronal electrical parameters are not likely to change over the time period of the recordings.

The membrane potential transitions from Down to Up states (Up transitions) and from Up to Down states (Down transitions), while short compared to the durations of the states themselves, are sufficiently long in duration to form a significant portion of the period of the membrane potential. Within a given neuron, these transitions normally occur in a highly stereotypical pattern (Stern et al., 1997). The durations of Up transitions were longer in neurons in transgenic mice than in controls (Figure 2E; $p = 0.002$, K-sample Anderson-Darling test; $p_{genotype} \approx 0$,

Genotype × Age ANOVA and $p < 0.05$, Tukey post-hoc test). Similar results were found for Down transitions in neurons in 3mo transgenic mice compared to controls (Figure 2F; $p = 0.018$, K-sample Anderson-Darling test; $p_{genotype} = 0.001$, Genotype × Age ANOVA and $p < 0.05$, Tukey post-hoc test). Up and Down transition durations were more variable within neurons in transgenic mice than those in controls (Figures 2E and 2F; Up transitions: $p_{genotype} \approx 0$, Down transitions: $p_{genotype} = 0.0062$, Genotype × Age ANOVA and $p < 0.05$, Tukey post-hoc test). The longer Up transitions found in transgenic mice could be induced by both intrinsic electrical properties of the membrane and the synaptic afferent barrage, yet the greater within-cell variability of the durations of Up transitions observed in these mice probably reflects a reduction in sufficient synchronous synaptic input, given the implausibility of changes in cell parameters occurring over the time of recording. The Down transitions are the response of the membrane potential to removal of synaptic inputs (Haider et al., 2006; Leger et al., 2005; Rudolph et al., 2007), and therefore reflect a change in the intrinsic electrical properties of the neurons. Thus, the longer average Down transitions observed in 3mo transgenic mice likely reflect changes in intrinsic mechanisms in these neurons, while the larger variability of their durations found in both transgenic groups may indicate a network effect. Taken together, these findings indicate a reduction in the number and/or synchrony of synaptic inputs in transgenic mice. In addition, our data may suggest changes in intrinsic electrical properties in 3mo transgenic mice, which may also be altered in 5mo transgenic mice, yet masked by more extreme synaptic effects. The observed increase in the average Down state duration, without a parallel change in the average Up state duration, in addition to the increase in state transition durations in transgenic mice, likely underlie the lower

neuronal oscillation frequency observed in these mice using both intracellular and extracellular recordings.

** Figure 2 about here **

Transgenic neurons showed an increase in the frequency of small depolarizing events in the Down state (false Up transitions), in which the membrane potential began a transition to Up state, but failed and returned to Down state (Figure 3A). Neurons in 5mo transgenic mice displayed a greater number of false Up transitions, and a smaller number of true Up transitions than controls (Figure 3B; false transitions: $p_{genotype} = 0.0007$, true transitions: $p_{genotype} = 0.0081$, Genotype × Age ANOVA and $p < 0.05$, Tukey post-hoc test), the latter consistent with our finding of a lower principal frequency of subthreshold membrane potential fluctuations. The longer intervals observed between successive (true) Up transitions in 5mo transgenic neurons compared to controls ($p_{genotype} = 0.0006$, Genotype × Age ANOVA and $p < 0.05$, Tukey post-hoc test) were not observed when false Up transitions were included in Up transition interval calculations, thus eliminating the difference between groups (Figure 3C; $p_{genotype} = 0.9$, Genotype × Age ANOVA and $p < 0.05$, Tukey post-hoc test). This indicates that false Up transitions portray a pathological tau-induced loss-of-function. The higher number of false Up transitions found in 5mo transgenic mice may be a consequence of the longer time they spent in Down state, allowing them a longer time window during which to emerge. To correct for this, we compared the proportion of false Up transitions among groups of neurons that had a comparable low principal frequency, and found the higher proportion of false Up transitions in transgenic mice to be maintained (Figure 3D).

Up states are caused by correlated synaptic input; therefore the observed reduction in successful Up states with a corresponding increase in Up transition failures, along with no observed changes in the electrical constants in the Down state, indicate a decrease in the number and/or synchrony of synaptic inputs in transgenic mice. The net result is a lowering of transmission reliability of synaptic information in the transgenic neocortex.

** Figure 3 about here **

The changes observed in subthreshold membrane potential dynamics would be expected to cause changes in the firing properties of the neuron, as APs arise only in Up states. APs are induced by a more stringent input timing pattern of afferent synchronous synaptic inputs than those generating the Up state, either by additional synchronous synaptic inputs (Leger et al., 2005) or by reduction of inhibitory inputs (Rudolph et al., 2007). We found no changes related to pathological tau in spike properties measured from intracellularly recorded neurons (Table S2), indicating basic electrical properties intrinsic to the neuron and conductances underlying AP generation are unaltered. We compared the firing rate of extracellularly recorded single units in 5mo transgenic mice and their age-matched controls during QW and SWS. During SWS, 5mo transgenic mice had a lower firing rate than controls ($p = 0.03$, t-test), while during QW no difference was observed (Figure 4A; $p = 0.12$, t-test). These findings indicate that pathological tau may disturb spiking activity mainly in epochs of high network synchronicity, such as SWS. Intracellular recordings under anesthesia revealed that neurons in transgenic mice had a lower spontaneous firing rate than those in controls ($p_{genotype} = 0.035$, Genotype × Age ANOVA and $p < 0.05$, Tukey post-hoc test), even when the firing rate was calculated solely within the Up states (Figure 4B; $p_{genotype} = 0.047$, Genotype × Age ANOVA and $p < 0.05$, Tukey

post-hoc test). These results suggest that the reduction of firing rate in transgenic neurons is governed by two separate mechanisms: the longer Down states, from which APs do not arise, and the reduced firing rates in the Up states. These findings also lend support to our claim of a pathological tau-induced reduction of firing rate during highly synchronized activity epochs.

To quantify the changes in firing patterns in intracellular recordings, we compared the firing pattern within Up states among groups. Neurons in 5mo transgenic mice had longer inter-spike intervals (ISIs) than controls (Figure 4C; $p_{genotype} = 0.026$, Genotype × Age ANOVA and $p < 0.05$, Tukey post-hoc test), and neurons in transgenic mice showed longer latencies to spike from Up transition than controls (Figure 4D; $p_{genotype} = 0.032$, Genotype × Age ANOVA and $p < 0.05$, Tukey post-hoc test). The changes in firing patterns within the Up state of transgenic neurons are not due solely to the changes in firing rate, as firing patterns differed between groups, even when compared using firing probability over time (Figure 4C).

It is unlikely that the changes in firing rates and patterns observed in transgenic neurons are a result of changes in electrical properties intrinsic to the neuron, as we found no changes related to pathological tau in the mean Up state voltage, spike properties or voltage trajectory leading to spikes (Tables S1 and S2), and no changes in firing rate during QW. The firing patterns observed in the intracellularly recorded neocortical neurons from transgenic mice, are driven by synaptic input resulting from spiking of afferent neurons which induce the recorded cells to rise to Up state and fire APs. However, the lower neuronal oscillation frequencies observed in transgenic mice during highly synchronized activity epochs, as KX anesthesia and SWS, suggest the reduced firing rates and altered firing patterns observed in transgenic neurons are

likely due to the changes in synaptic input patterns to these cells, such as lower overall input and/or lower overall synchrony.

** Figure 4 about here **

DISCUSSION

We have demonstrated, in the first *in vivo* intracellular and extracellular study of an animal model of tauopathy, that pathological tau reduces the activity of single neocortical pyramidal cells and of the neocortical network. Using intracellular recordings in anesthetized mice, we found a lower degree of background activity in neurons in transgenic mice, reflected in altered patterns of both subthreshold membrane potential dynamics and spiking activity. Using extracellular recordings, we found a reduction in the dominant oscillatory frequency of the local field potentials in transgenic mice during SWS, as well as lower firing rates. Our main findings differ from those of *in vitro* intracellular studies (Crimins et al., 2012; Crimins et al., 2011; Rocher et al., 2009), probably due to the inherent differences between *in vivo* and *in vitro* preparations and recording techniques.

This study was conducted in the rTg4510 mouse model of tauopathy, overexpressing human tau with the dementia-associated P301L mutation (Hutton et al., 1998). This is a well characterized (Ramsden et al., 2005; Santacruz et al., 2005; Spires et al., 2006), widely used and accepted animal model of tauopathy (Cheng and Ji, 2013; Crimins et al., 2012; Hoover et al., 2010; Kopeikina et al., 2013). While this mutation has not been identified in Alzheimer's disease, and despite the diverse phenotype and distinct clinical presentations of different neurodegenerative tauopathies, the common progressive accumulation of NFTs in tauopathies suggests a

common mechanism of disease pathogenesis (Gendron and Petrucelli, 2009), and validates the rTg4510 mouse strain as its model.

Findings from extracellular recordings in freely behaving mice and intracellular recordings in anesthetized mice both indicate lowered neuronal oscillation frequency and reduced firing rates. The former method, but not the latter, is free from possible differential effects of anesthesia and intracellular-pipette damage, and allows a much better sampling of activity of neuronal populations. Therefore, taken together, these complementary findings from both methods imply that pathological tau alters the functional connectivity of the cortical network in a manner that disrupts highly synchronous epochs of activity, such as KX anesthesia and SWS, but is negligible during less synchronized epochs, as QW.

Our findings of altered activity in neurons in transgenic mice are most likely attributable to synaptic input insufficiency; i.e. the lack of enough inputs synchronized within a specific time window (determined by postsynaptic membrane time constants) to elicit and maintain an Up state and generate normal firing patterns (Bernander et al., 1991; Leger et al., 2005). The insufficiency may be due to a number of non-mutually-exclusive causes: reduction of synaptic inputs caused by neuronal and/or synaptic degeneration; synaptic failure caused by impaired cellular trafficking, a decrease in the correlation of the synaptic inputs onto the postsynaptic neuron, or a combination of these factors. Our study could not distinguish between these possible mechanisms. The reduction in the principal frequency of membrane potential dynamics found during anesthesia and SWS in transgenic mice, as well as the longer durations of Down states and rise times to Up states, along with the observed reduction in successful Up states and increase in false Up transitions, all indicate a decrease in the number and/or synchrony of synaptic inputs to these neurons. In

addition, the larger within-cell variability found in Down state durations and in rise times to Up states, along with no observed changes in Up state durations or in basic electrical parameters (such as input resistance, time constant and resting membrane potential), support the claim that the basic biophysical properties of the neurons were intact in transgenic mice and are unlikely to be the cause of the alterations in their activity. The differences found in firing rate and patterns in neurons in transgenic mice, using intracellular and extracellular recordings during anesthesia and SWS respectively, along with no observed differences in spike properties, lend further support to our claim.

It should be noted that these changes occur at ages with no appreciable cell death (Figure S1; Santacruz et al., 2005; Spires et al., 2006) or distinct spine or synapse loss (Crimins et al., 2012; Hoover et al., 2010; Kopeikina et al., 2013). Although one study has indicated miss-sorting of mutant tau into dendritic spines in the 5mo transgenic mice group (Hoover et al., 2010), it is unlikely that such changes could underlie the degree of synaptic insufficiency observed in this study. Taken together with unchanged firing rates during QW, these findings suggest that the underlying synaptic input insufficiency is mainly caused by a reduction in synaptic synchrony, and to a lesser extent by a reduction in the number of synaptic inputs. These mechanisms may involve impaired cellular trafficking (Kopeikina et al., 2011) and possible changes to neuritic architecture (Rocher et al., 2009; Crimins et al., 2011; Crimins et al., 2012).

Our study has not differentiated between the effects of soluble tau and NFTs on neocortical neuronal activity. We have established that the neocortical activity of 5mo transgenics is affected to a greater extent than that of 3mo transgenics, with the former displaying significantly higher levels of NFT aggregation than the latter.

Unfortunately, we could not recover all recorded neurons to unequivocally show that not all of them were burdened by pathological tau. However, our findings indicate that only a fraction of neurons are directly affected by NFTs in the investigated age cohorts, in accordance with previously published findings (Glat et al., 2013; Spires et al., 2006). Given these statistics, it is unlikely that our recordings were exclusively from neurons bearing NFTs. Thus, we suggest the altered activity observed in neocortical neurons in 5mo transgenic mice does not depend on whether the individual recorded neuron contains an NFT, as also corroborated by *in vitro* studies (Crimins et al., 2012; Crimins et al., 2011; Rocher et al., 2009). Since soluble tau is also increased at this age, it is reasonable to assume that this tau species also affects neuronal activity. However, the possibility exists that pathological tau affects neuronal activity at levels below that of detections with the immunocytochemical methods used in this study. We therefore cannot rule out the possibility that many more neurons have accumulated pathological tau than we can detect.

Our results reveal a global reduction in activity, likely caused by pathological-tau-affected individual neurons, which reduce the activity of downstream unaffected neurons. A possible mechanism could be morphological changes of tau-affected neurons (Crimins et al., 2012; Crimins et al., 2011; DeKosky and Scheff, 1990; Hoover et al., 2010; Knowles et al., 1999; Kopeikina et al., 2011; Kopeikina et al., 2013; Moreno et al., 2011; Rocher et al., 2009; Roy et al., 2005; Shemesh et al., 2008; Stamer et al., 2002; Stokin et al., 2005; Yoshiyama et al., 2007), leading to disruption of information transmission, first in these neurons and their direct contacts, and gradually proliferating throughout the tau-burdened neocortical network, eventually leading to global synaptic insufficiency. A reduction in synaptic synchrony or, less likely, in the number of synaptic inputs, as revealed by the changes in subthreshold

membrane potential fluctuation patterns and the lower principal oscillatory frequencies, while allowing for partial function of the cortical neurons, significantly changes the firing patterns and spike rates of these cells. Such changes will inevitably affect the fine scale of the neurons' ability to encode multidimensional information by complex patterns of spike trains. This finding may explain the discrepancy between the evidence for functional integration of tangle-bearing neurons in visual cortex (Kuchibhotla et al., 2014), and, on the other hand, cognitive dysfunction (Santacruz et al., 2005; Crimins et al., 2011). Neurons may show normal tuning to stimulus parameters when integrating over a long period of time, while fine structure of neuronal activity, on the millisecond time scale, is disrupted. This fine structure of spike activity is at least partially generated by the complex spatiotemporal patterns of inputs to the cell, and can encode essential parameters of the inputs (Las et al., 2005). Our study has shown a disruption in this pattern of inputs, regardless of whether the recorded neuron bears NFTs. We suggest that such a reduction in global neuronal activity caused by neuropathology in a subset of the affected network, prior to substantial neurodegeneration, may explain the cognitive decline characteristic of human tauopathy and Alzheimer's Disease.

REFERENCES

Abeles, M. (1982). Quantification, smoothing, and confidence limits for single-units' histograms. J Neurosci Methods 5, 317-325.

Arieli, A., Sterkin, A., Grinvald, A., and Aertsen, A. (1996). Dynamics of ongoing activity: explanation of the large variability in evoked cortical responses. Science 273, 1868-1871.

Avila, J., Lucas, J.J., Perez, M., and Hernandez, F. (2004). Role of tau protein in both physiological and pathological conditions. Physiol Rev 84, 361-384.

Bartho, P., Hirase, H., Monconduit, L., Zugaro, M., Harris, K.D., and Buzsaki, G. (2004). Characterization of neocortical principal cells and interneurons by network interactions and extracellular features. Journal of neurophysiology 92, 600-608.

Bernander, O., Douglas, R.J., Martin, K.A., and Koch, C. (1991). Synaptic background activity influences spatiotemporal integration in single pyramidal cells. Proc Natl Acad Sci U S A 88, 11569-11573.

Chauvette, S., Crochet, S., Volgushev, M., and Timofeev, I. (2011). Properties of slow oscillation during slow-wave sleep and anesthesia in cats. J Neurosci 31, 14998-15008.

Cheng, J., and Ji, D. (2013). Rigid firing sequences undermine spatial memory codes in a neurodegenerative mouse model. eLife 2, e00647.

Connors, B.W., and Gutnick, M.J. (1990). Intrinsic firing patterns of diverse neocortical neurons. Trends Neurosci 13, 99-104.

Connors, B.W., Gutnick, M.J., and Prince, D.A. (1982). Electrophysiological properties of neocortical neurons in vitro. Journal of neurophysiology 48, 1302-1320.

Costa, R.M., Cohen, D., and Nicolelis, M.A. (2004). Differential corticostriatal plasticity during fast and slow motor skill learning in mice. Curr Biol 14, 1124-1134.

Cowan, R.L., and Wilson, C.J. (1994). Spontaneous firing patterns and axonal projections of single corticostriatal neurons in the rat medial agranular cortex. Journal of neurophysiology 71, 17-32.

Crimins, J.L., Rocher, A.B., and Luebke, J.I. (2012). Electrophysiological changes precede morphological changes to frontal cortical pyramidal neurons in the rTg4510 mouse model of progressive tauopathy. Acta Neuropathol 124, 777-795.

Crimins, J.L., Rocher, A.B., Peters, A., Shultz, P., Lewis, J., and Luebke, J.I. (2011). Homeostatic responses by surviving cortical pyramidal cells in neurodegenerative tauopathy. Acta Neuropathol 122, 551-564.

DeKosky, S.T., and Scheff, S.W. (1990). Synapse loss in frontal cortex biopsies in Alzheimer's disease: correlation with cognitive severity. Ann Neurol 27, 457-464.

Gendron, T.F., and Petrucelli, L. (2009). The role of tau in neurodegeneration. Mol Neurodegener 4, 13.

Gervasoni, D., Lin, S.C., Ribeiro, S., Soares, E.S., Pantoja, J., and Nicolelis, M.A. (2004). Global forebrain dynamics predict rat behavioral states and their transitions. J Neurosci 24, 11137-11147.

Glat, M., Skaat, H., Menkes-Caspi, N., Margel, S., and Stern, E.A. (2013). Age-dependent effects of microglial inhibition in vivo on Alzheimer's disease

neuropathology using bioactive-conjugated iron oxide nanoparticles. Journal of nanobiotechnology 11, 32.

Haider, B., Duque, A., Hasenstaub, A.R., and McCormick, D.A. (2006). Neocortical network activity in vivo is generated through a dynamic balance of excitation and inhibition. J Neurosci 26, 4535-4545.

Hof, P.R., Young, W.G., Bloom, F.E., Belichenko, P.V., and Celio, M.R. (2000). Comparative Cytoarchitectonic Atlas of the C57BL/6 and 129/Sv Mouse Brains (Amsterdam: Elsevier Health Sciences).

Hoover, B.R., Reed, M.N., Su, J., Penrod, R.D., Kotilinek, L.A., Grant, M.K., Pitstick, R., Carlson, G.A., Lanier, L.M., Yuan, L.L., *et al.* (2010). Tau mislocalization to dendritic spines mediates synaptic dysfunction independently of neurodegeneration. Neuron 68, 1067-1081.

Kellner, V., Menkes-Caspi, N., Beker, S., and Stern, E.A. (2014). Amyloid-beta alters ongoing neuronal activity and excitability in the frontal cortex. Neurobiol Aging 35, 1982-1991.

Knowles, R.B., Wyart, C., Buldyrev, S.V., Cruz, L., Urbanc, B., Hasselmo, M.E., Stanley, H.E., and Hyman, B.T. (1999). Plaque-induced neurite abnormalities: implications for disruption of neural networks in Alzheimer's disease. Proc Natl Acad Sci U S A 96, 5274-5279.

Kopeikina, K.J., Carlson, G.A., Pitstick, R., Ludvigson, A.E., Peters, A., Luebke, J.I., Koffie, R.M., Frosch, M.P., Hyman, B.T., and Spires-Jones, T.L. (2011). Tau accumulation causes mitochondrial distribution deficits in neurons in a mouse model of tauopathy and in human Alzheimer's disease brain. Am J Pathol 179, 2071-2082.

Kopeikina, K.J., Polydoro, M., Tai, H.C., Yaeger, E., Carlson, G.A., Pitstick, R., Hyman, B.T., and Spires-Jones, T.L. (2013). Synaptic alterations in the rTg4510 mouse model of tauopathy. The Journal of comparative neurology 521, 1334-1353.

Leger, J.F., Stern, E.A., Aertsen, A., and Heck, D. (2005). Synaptic integration in rat frontal cortex shaped by network activity. Journal of neurophysiology 93, 281-293.

McCormick, D.A., Connors, B.W., Lighthall, J.W., and Prince, D.A. (1985). Comparative electrophysiology of pyramidal and sparsely spiny stellate neurons of the neocortex. Journal of neurophysiology 54, 782-806.

Moreno, H., Choi, S., Yu, E., Brusco, J., Avila, J., Moreira, J.E., Sugimori, M., and Llinas, R.R. (2011). Blocking Effects of Human Tau on Squid Giant Synapse Transmission and Its Prevention by T-817 MA. Frontiers in synaptic neuroscience 3, 3.

Rocher, A.B., Crimins, J.L., Amatrudo, J.M., Kinson, M.S., Todd-Brown, M.A., Lewis, J., and Luebke, J.I. (2009). Structural and functional changes in tau mutant mice neurons are not linked to the presence of NFTs. Exp Neurol.

Roy, S., Zhang, B., Lee, V.M., and Trojanowski, J.Q. (2005). Axonal transport defects: a common theme in neurodegenerative diseases. Acta Neuropathol 109, 5-13.

Rudolph, M., Pospischil, M., Timofeev, I., and Destexhe, A. (2007). Inhibition determines membrane potential dynamics and controls action potential generation in awake and sleeping cat cortex. J Neurosci 27, 5280-5290.

Santacruz, K., Lewis, J., Spires, T., Paulson, J., Kotilinek, L., Ingelsson, M., Guimaraes, A., DeTure, M., Ramsden, M., McGowan, E., *et al.* (2005). Tau

suppression in a neurodegenerative mouse model improves memory function. Science 309, 476-481.

Shemesh, O.A., Erez, H., Ginzburg, I., and Spira, M.E. (2008). Tau-induced traffic jams reflect organelles accumulation at points of microtubule polar mismatching. Traffic 9, 458-471.

Spires, T.L., Orne, J.D., SantaCruz, K., Pitstick, R., Carlson, G.A., Ashe, K.H., and Hyman, B.T. (2006). Region-specific dissociation of neuronal loss and neurofibrillary pathology in a mouse model of tauopathy. Am J Pathol 168, 1598-1607.

Stamer, K., Vogel, R., Thies, E., Mandelkow, E., and Mandelkow, E.M. (2002). Tau blocks traffic of organelles, neurofilaments, and APP vesicles in neurons and enhances oxidative stress. The Journal of cell biology 156, 1051-1063.

Steriade, M., Nunez, A., and Amzica, F. (1993). A novel slow (< 1 Hz) oscillation of neocortical neurons in vivo: depolarizing and hyperpolarizing components. J Neurosci 13, 3252-3265.

Stern, E.A., Kincaid, A.E., and Wilson, C.J. (1997). Spontaneous subthreshold membrane potential fluctuations and action potential variability of rat corticostriatal and striatal neurons in vivo. Journal of neurophysiology 77, 1697-1715.

Stokin, G.B., Lillo, C., Falzone, T.L., Brusch, R.G., Rockenstein, E., Mount, S.L., Raman, R., Davies, P., Masliah, E., Williams, D.S., and Goldstein, L.S. (2005). Axonopathy and transport deficits early in the pathogenesis of Alzheimer's disease. Science 307, 1282-1288.

Thies, E., and Mandelkow, E.M. (2007). Missorting of tau in neurons causes degeneration of synapses that can be rescued by the kinase MARK2/Par-1. J Neurosci 27, 2896-2907.

Yoshiyama, Y., Higuchi, M., Zhang, B., Huang, S.M., Iwata, N., Saido, T.C., Maeda, J., Suhara, T., Trojanowski, J.Q., and Lee, V.M. (2007). Synapse loss and microglial activation precede tangles in a P301S tauopathy mouse model. Neuron 53, 337-351.

Acknowledgements: We are grateful to Dr. Jada Lewis for granting permission to use the rTg4510 mice, and to Prof. George Carlson and Ms. Rose Pitstick for kindly providing them. We thank Dr. Peter Davies for kindly providing PHF1 and Alz50 antibodies, and Dr. Shih-Chieh Lin for kindly providing the Matlab code for construction of a two-dimensional state space. We thank Profs. Bradley T. Hyman and Israel Nelken for critical reading of the manuscript. We declare no conflict of interests.

EXPERIMENTAL PROCEDURES

Animals

We used the well-characterized rTg4510 mouse model of tauopathy (provided by Jada Lewis and George Carlson), in which transgenic mice for tau responder and activator transgenes overexpress the human four-repeat tau gene carrying the frontotemporal dementia-associated P301L mutation (Santacruz 2005; Ramsden 2005). Transgenic mice were used in two age cohorts in this study: 3-3.5 months old mice ("3mo") and 4.5-6 months old mice ("5mo"), both displaying accumulations of hyperphosphorylated and misfolded tau and mature NFTs in the neocortex, with the latter showing significantly higher levels of NFT aggregation, yet prior to appreciable cell death; in agreement with previously published findings (Ramsden et al., 2005; Santacruz et al., 2005; Spires et al., 2006). Age-matched littermates that do not express tau were used as controls. No differences were observed between control mice lacking the tau responder transgene and those lacking the activator transgene in central physiological parameters. In addition, a previous study reported no differences between these control groups in pathological parameters (Spires et al., 2006). Therefore, data from mice of the same age group with different control genotypes were pooled into a single age-matched control group.

All procedures were approved by the Bar-Ilan University Animal Care and Use Committee and performed in accordance with Israeli Ministry of Health and US National Institutes of Health (NIH) guidelines. All animals were housed on a 12:12 hour light/dark cycle and had ad libitum access to food and water.

In vivo intracellular recordings in anesthetized animals

Intracellular *in vivo* recordings were performed from 22 female mice and 17 males. No differences were found between mice of different sex.

Surgical procedure. The surgical procedure has been described in detail elsewhere (Kellner et al., 2014). In brief, mice were anesthetized with ketamine–xylazine (130 and 10 mg/kg, respectively) and placed in a custom-built stereotaxic device. During surgery and recording, mice were given supplemental injections to maintain anesthesia level. Small holes were drilled for electrocorticogram (ECoG) electrodes and a stabilization screw above the cortex and cerebellum. Methods for reduction of brain pulsations (opening of a cisternal drain and suspension by clamp at the tail base) were not used, due to instability of the brain preparation in transgenic mice. All animals continued to breathe without artificial respiration. A ~2×1 mm^2 craniotomy was opened over the frontal pole of the left hemisphere of the cortex (central coordinates: +1.4 mm AP, 0.6 mm ML) and the dura was removed. Recording electrodes (1.5 mm outer diameter, 0.86 mm inner diameter, glass; A-M systems, Sequim, WA) were filled with 1 M potassium acetate and either 4% Biocytin (Sigma-Aldrich, St. Louis, MO), Alexa-Fluor 594-biocytin or Alexa-Fluor 594 Hydrazide (Molecular Probes, Eugene, OR) for cell visualization. Electrode resistance measured 30-100 MΩ in PBS. Depth of all electrophysiological recordings ranged from 104 μm to 1496 μm with no significant differences between the experimental groups in recording depths ($p_{genotype}$ = 0.0793, Genotype × Age ANOVA). Within the analyzed database, we found no significant correlations between the recording depth of the neuron and principal parameters investigated in the present work for a Bonferroni-corrected p-value for multiple comparisons.

Data acquisition. A high-impedance amplifier with active bridge circuitry (IR-283; Cygnus Technology, Southport, NC) was used for recording. Data was acquired via A/D board (Power 1401 mkII; Cambridge Electronic Design, Cambridge, UK) using custom scripts in Spike2/Signal (Cambridge Electronic Design) at 10 kHz.

Impaled cells were tentatively identified online, during recording, as pyramidal neurons, using known physiological characteristics (Connors and Gutnick, 1990; Connors et al., 1982; McCormick et al., 1985) and criteria of distinguishable Up and Down states with average voltage differences of at least 10 mV and healthy action potentials (APs or spikes) with an amplitude exceeding 50mV. Cells that had characteristics of fast-spiking neurons were not used in this study. When a neuron was impaled, spontaneous (i.e., ongoing) activity was recorded for 1-5 minutes, and were segmented into 1-minute traces. The traces were analyzed separately and then averaged within the neuron, to ensure averaging of non-stationary events. For a subset of neurons, current–voltage responses were measured as well, in order to quantify intrinsic electrophysiological properties, such as: input resistance and membrane time constant. Cells were stimulated with 220 ms long square current pulses via the recording electrode. Each current intensity was applied eight times, and ranged from -1 nA to 1 nA with 0.05 nA steps. Data were analyzed offline using Matlab (R2010b; MathWorks Inc., Natick, MA) and Excel (Microsoft Office, Redmond, WA). The voltage measured just outside the recorded neuron ("DC shift" or tip potential) was subtracted from the measured membrane potential of the neuron at an early stage of analysis.

Histology. Following a transcardial perfusion (4% paraformaldehyde in PBS), brains were post-fixed for at least 24 hours, cryoprotected, frozen and then cut into 25-50 µm thick sections. Sections containing recorded neurons were stained with 0.05% Thioflavin-S (ThioS; Sigma-Aldrich) in 50% ethanol to reveal NFTs. NFTs and neurons were retrieved using a Nikon fluorescent microscope.

In vivo extracellular recordings in freely behaving animals

Extracellular *in vivo* LFPs were recorded from four 5mo transgenic mice and seven age-matched controls. Single units were recorded from a subset of three 5mo transgenic mice and three age-matched controls. All mice were male, except for one female transgenic mouse.

Behavioral analysis. Mice were individually housed in a clean cage (17cm × 29cm × 14cm, for width, length and height, respectively) with a small amount of bedding for 24 hours before the recording session to familiarize them with their recording cage. At the day of the experiment, the mouse was connected to the head stage for at least 30 minutes prior to the start of the recordings to enable habituation to the recording wires and the experimenter's presence. Each experimental session included about 3 hours of recording, during which a well-trained experimenter encoded the animal's behavioral states by visual observation of behaviors and associated LFP spectral features as previously described in (Gervasoni et al., 2004). Briefly, three behavioral states were encoded in this study: (1) Quiet wakefulness (QW) in which the animal was immobile in the cage, (2) Active exploration (AE), and (3) Slow-wave sleep (SWS) in which the animal was laying with its eyes closed while the LFP showed high amplitude waves in the delta range (1-4 Hz).

Surgical procedure. The surgical procedure has been described in detail elsewhere (Costa et al., 2004). In brief, a ~2×1 mm^2 craniotomy was made over the frontal cortex (AP: 0.3-2.3; ML: 1-2); custom made microwire arrays (4×4 or 4×8 arrays of S-isonel-coated tungsten microwires of 35 or 50 µm in diameter) were lowered by 700-800 µm from the surface of the brain (Hof et al., 2000) while recording neuronal activity. Final placement of the electrodes was decided based on the coordinates and quality of neural activity and confirmed histologically after

electrolytic marking lesions, perfusion and brain fixation with 4% paraformaldehyde in PBS followed by sectioning into 50 µm thick slices.

Data acquisition. We chronically recorded neural activity from the frontal cortex using microwire arrays. Neural activity was amplified, band-pass filtered at 150-8000 Hz and sampled at 40 KHz using a multichannel acquisition processor system (MAP system; Plexon, Dallas, TX). The activity was initially sorted online; however all waveforms exceeding a selected threshold were saved for offline sorting (OfflineSorter V2.8.8; Plexon). Only confirmed single units with a signal to noise ratio above 3:1 were further analyzed using custom-written MATLAB software. During the sorting procedure we made sure that a single neuron is not included in the analysis twice. LFPs were preamplified (250×), lowpass filtered (200 Hz), and digitized at 1000 Hz using a Digital Acquisition card (National Instruments, Austin, TX) and a MAP (Plexon).

Statistics

Alpha was defined as 0.05 for all tests. For intracellular recordings, significance was tested using a Genotype × Age analysis of variance (ANOVA) design, followed by post-hoc analyses using Tukey's honestly significant difference criterion. A permutation test was employed on the ANOVA tests to confirm the validity of the Fscore. For extracellular recordings, significance was tested using a student's t-test. However, in several cases, different statistical tests were employed.

Data analysis

For each analysis, outliers were determined and removed by creating a cutoff value at the mean ± 2.58 × standard deviations of the group mean value (Abeles, 1982).

Subthreshold membrane potential states

In order to classify the different states of the intracellularly recorded membrane potential (Down and Up), we constructed all-points (voltage distribution) histograms (APH) for each 60-s trace using 1mV bins. Spikes peaks were detected by local maxima from a threshold of -30mV and spike times were stored for further analyses of spiking activity. Spikes were clipped and replaced with the membrane potential value at spike threshold. .Next, the trace was downsampled to 1 kHz, and the frequencies of different values of the membrane potential were binned and normalized to probability units. The peaks of the bimodal distribution displayed in the APH represent the modes of the Up and Down states. The minimum of the APH was defined as the separation point between the two states and the transition points to each state were set as 2/3 of the way between the separation point and the state mode (see also (Stern et al., 1997)). The trace was then filtered using a finite impulse response (FIR) low-pass filter of order 100 with 40 Hz cutoff frequency. Each data point was classified as an Up state, Down state, or a state transition: Rise to Up state (Up transition) or Fall to Down state (Down transition). State durations were defined as the difference (in milliseconds) between the time of transition points to Up/Down states and the time these states ended. Transition durations were defined as the differences between the time when one state ended (Down/Up) and the time the following alternate state began (Up/Down).

Subthreshold membrane potential fluctuations

We measured the average oscillatory cycles of the intracellularly recorded spontaneous membrane potential fluctuations using two different methods. We measured the time interval between successive Up transition points, essentially measuring the duration between adjacent Up states. We constructed a histogram of the Up-Up state interval distribution and calculated the mean interval for each cell. We

also calculated the mean squared spectrum using Welch's method (*pwelch* Matlab function) for one 60-s trace from each neuron. Each trace was windowed with a Hamming window and parameters were selected to enable a 0.12 Hz frequency resolution. The log power for each frequency was normalized by the power in 200-300 Hz, and averaged for each genotype group. The frequency at maximum power was identified as the principal frequency of the cell, i.e. the frequency of the slow membrane potential oscillations between Up and Down states.

Identification of SWS and QW epochs

Visually encoded SWS and QW time epochs were verified using a two-dimensional state space constructed as previously described (Gervasoni et al., 2004). Matlab code for generating the maps was kindly provided by the authors. Briefly, state space was defined by two spectral amplitude ratios calculated by dividing integrated spectral amplitudes at selected frequency bands from LFPs simultaneously recorded from different electrodes. The selected frequency bands are 0.5–20/0.5–55 Hz for ratio 1 and 0.5– 4.5/0.5–9 Hz for ratio 2. These two ratios were used to construct the 2-D state space in which each point represents 1 second of ongoing brain activity (Figure S2)The positions of the different states, i.e. QW and SWS, in the state map were valid and well preserved across mice, as previously described (Gervasoni et al., 2004).

Removal of FSIs from extracellular data

Spike valley to peak duration was calculated for each neuron (see below) and used as a criterion to remove presumably fast spiking interneurons (Bartho et al., 2004). Compatible with previous reports (Bartho et al., 2004), we removed units with valley to peak duration < 350 micron (4 units from each genotype removed).

Spike valley to peak duration from extracellular data

Spike waveform was segmented from 200 microseconds prior to crossing the spike threshold to 600 microseconds following it. We verified that the global extramum of all spikes are negative, by multiplying the waveform by -1 if necessary, and then calculated the spike valley to peak duration from its minimum to maximum amplitude.

Power spectrum analysis of LFP

One representative LFP channel was selected for analysis per session. The mean squared spectrum was calculated using Welch's method (*pwelch* Matlab function). Each LFP section was windowed with a Hamming window and parameters were selected to enable a 0.5 Hz frequency resolution. The log power for each frequency was normalized by the power in 200-300 Hz, and averaged over SWS / QW epochs for each genotype group. To measure the differences in the PSDs of transgenic and control mice we used two different measures. The first measure was the frequency at maximum power, which was identified as the principal frequency. The second measure was the spindle-delta power ratio. To quantify the difference between the delta (1-4 Hz) and the spindle (7-14 Hz) frequency ranges among groups, we calculated the normalized power in each range: $\frac{sum(power\ in\ range)}{frequency\ range}$, and divided the normalized ratios of the two frequency ranges. The closer this value is to 1, the more similar the selected frequency ranges are in their normalized power.

False state transitions

Failures to transition to the Up state (false Up transitions) were defined as small depolarizing events in the Down state, in which the intracellularly recorded membrane potential ascended out of the Down state confidence interval, but failed to reach the Up state transition point and returned to the Down state. Confidence intervals for Up

and Down states were defined as the difference between the average Up/Down state value and 2.58 times the standard deviation of the voltage in that state (Abeles, 1982). We counted the number of instances of failed transitions in each 60-seconds trace and averaged it within the cell. To accurately compare false Up transition frequency across groups, the frequency of each cell was normalized by the sum of its true and false Up transitions to yield the proportion of false Up transitions. A similar calculation was used for false Down transitions.

Passive electrical properties

In order to determine the passive electrical properties of the intracellularly recorded neurons in the different groups, we measured the voltage responses of each neuron, in a subset of cells, to applied square current steps (-1 nA to 1 nA with 0.05 nA steps) at 50 ms after current pulse injection. For each current step, we averaged the membrane potential value during eight pulse applications of the same current intensity to ensure averaging of non-stationary events, and constructed current-voltage curves (*I-V*). Voltage responses were sorted according to the subthreshold state (Up/Down) of the membrane potential at 20 ms prior to current application. The mode of the membrane potential of the state was subtracted from the response to reduce variability arising from different baseline membrane potential values, and state-specific current-voltage curves (*I-V*) were constructed as well (i.e., *I-V* curve for Down / Up states). Input resistance was determined for each neuron by calculating the slope of the fitted line to the linear portion (between -0.2 nA and 0.2 nA) of the *I-V* curve. The membrane time constant of each neuron was calculated by estimating the period of time by which the average voltage response to a current pulse of -0.2nA decayed to 37% of its initial value.

Firing rate and pattern

For intracellularly recorded neurons, we calculated the firing rate over the whole trace by dividing the number of spikes by the total length of the trace (60-seconds). Firing rate within Up states was calculated by dividing the number of spikes by the duration of the Up state (in seconds). Cells that did not fire at all were excluded from this analysis. Inter-spike intervals (ISIs) were calculated for each Up state within a neuron and then averaged over all Up states of that neuron**.** The average ISI histogram for each group was divided by the total number of ISIs for that group to give probability values. We also constructed histograms of the latency to spike from Up state transition time and calculated the average latency for each cell. Neurons with less than 10 spikes per trace were excluded from firing pattern analyses.

For extracellularly recorded neurons, firing rate was calculated in 5-minute traces of recording as the number of spikes emitted by the unit divided by the total recording time (~300s).

Spike properties

Spike properties were calculated per spike, and then averaged over the trace, and over the cell. Spike threshold was calculated as the point at which the second derivative of the membrane potential was maximal. Spike amplitude was defined as the voltage difference between the peak of the spike and the spike threshold. Half width was calculated as the duration of the width of the spike at half its amplitude (between peak and spike threshold). Trajectory to spike was defined as the voltage difference between the spike threshold and the membrane potential 10 ms prior to it, delineating the depolarization course of the membrane potential to reach spike threshold value. Neurons with less than 10 spikes per trace of ongoing activity were excluded from these analyses.

FIGURE LEGENDS

Fig. 1.Transgenic mice show spontaneous neuronal oscillations and AP firing in neocortex.

(**A**) Neurons and pathology in 5mo transgenic neocortex. Cells (yellow arrows) were recorded intracellularly and labeled *in vivo* (left). NFTs (white arrows) were stained in slices (center). In merged image (right), an NFT is present in the soma of one of the stained cells. Scale bar, 10 µm. **(B and C)** Representative intracellular *in vivo* recordings in neurons of 5mo control **(B)** and transgenic **(C)** mice. All-points-histograms (insets) represent the voltage distribution of subthreshold membrane potential. The bimodal distribution of the membrane potential is fit to a curve of a sum-of-2-Gaussians (red curve). Scale bar applies to intracellular voltage traces. **(D)** Verification of extracellular electrode placement in frontal pole of mice. Example of a 50 µm coronal slice showing electrode placement (arrow) in the frontal cortex of a 5mo transgenic mouse (left) following electrolytic lesion. Scale bar, 500 µm. Appropriate coronal section from atlas (right; Hof et al., 2000). Scale bar, 600 µm. **(E and F)** Representative extracellular *in vivo* recordings in neurons of 5mo control **(E)** and transgenic **(F)** mice. Average (+SEM) waveforms of neocortical pyramidal neurons recorded extracellularly from 5mo control **(E, left)** and transgenic **(F, left)** mice reveal the similarity in waveform parameters between both groups. Scale bar, 100 µs. Representative LFP recordings from 5mo control **(E, right)** and transgenic **(F, right)** neocortex during QW (top trace) and SWS (bottom trace). Scale bar, 1 s. See also Table S1 and Figures S1 and S2.

Fig. 2. Oscillations of transgenic neurons are slower than controls during SWS and anesthesia.

(A) Cumulative distribution function (CDF) of mean interval between successive Up transitions calculated from intracellular recordings under anesthesia showed longer Up-Up intervals in transgenic neurons. **(B)** Power spectral analysis of the membrane potential (mean ± SEM) revealed a slower mean (+SEM) principal frequency (inset) for neurons in 5mo transgenic mice compared with controls. Ctrl 3mo: n = 18 neurons from 11 mice; Ctrl 5mo: n = 20 neurons from 11 mice; Tg 3mo: n = 13 neurons from 8 mice; Tg 5mo: n = 12 neurons from 9 mice. **(C)** Power spectral analysis of LFP recordings (mean ± SEM) during QW (top left) and SWS (top right). PSD of 5mo transgenic mice (red) showed peaks only in the delta range, while controls showed two peaks, in the delta range and the spindle range (shaded). The mean (+SEM) spindle-delta power ratio was reduced for neurons in 5mo transgenic mice as compared with controls during both behavioral states (bottom left). Transgenic mice had a slower mean (+SEM) principal frequency as compared with controls during SWS, but not during QW (bottom right). Ctrl 5mo: n = 16 neurons from 3 mice; Tg 5mo: n = 10 neurons from 3 mice. **(D-F)** CDFs of mean Down state durations (D, left), rise times to Up state (E, left) and fall times to Down state (F, left), revealed longer durations of Down states and state transitions in transgenic neurons. Scatterplots (D-F, right) display the mean within-cell variability of the time spent in state / transition versus the mean time spent in state / transition for each group, and also reveal increased within-cell variability in transgenic neurons. Between-cell variability is depicted as SEM by the error bars. Ctrl young: n = 16,17,17 neurons from 9,10,10 mice respectively; Ctrl old: n = 19,19,20 neurons from 11,10,11 mice respectively; Tg young: n = 12,13,13 neurons from 7 mice; Tg old: n = 11,12,11 neurons from 9 mice. * $p < 0.05$.

Fig. 3. Neurons in 5mo transgenic mice have a higher proportion of false Up transitions than controls.

(A) Example of false Up transitions (arrowheads) identification in an intracellular recording of a neuron from a 5mo transgenic mouse, following removal of APs and down sampling of recorded trace. False Up transitions are small depolarizing events in the Down state, in which the intracellularly recorded membrane potential ascended out of the Down state confidence interval (shaded green), but failed to reach the Up state transition point and returned to the Down state. Up state confidence interval (shaded purple) was used for calculation of false Down states (not indicated). **(B)** Mean (+SEM) number of false (left) or true (i.e. Up states; right) Up transitions revealed a difference between neurons in 5mo transgenic mice and controls. Ctrl 3mo: n = 18 neurons from 10 mice; Ctrl 5mo: n = 19 neurons from 11 mice; Tg 3mo: n = 13 neurons from 8 mice; Tg 5mo: n = 12 neurons from 9 mice. **(C)** Mean (+SEM) intervals between successive true Up transitions (left) and all (true and false) Up transitions (right) revealed that the longer average interval of neurons in transgenic mice was reduced to that of controls when false Up transitions were included in interval calculation. Ctrl 3mo: n = 17 neurons from 10 mice; Ctrl 5mo: n = 19,20 neurons from 11 mice; Tg 3mo: n = 13,12 neurons from 8 mice; Tg 5mo: n = 12 neurons from 9 mice. **(D)** Scatterplot revealed that higher proportion of false Up transitions in transgenic neurons is maintained when compared with controls at a low principal frequency (shaded). Each dot represents a single cell color-coded for each group. Ctrl 3mo: n = 18 neurons from 11 mice; Ctrl 5mo: n = 20 neurons from 11 mice; Tg 3mo: n = 13 neurons from 8 mice; Tg 5mo: n = 12 neurons from 9 mice. * $p < 0.05$.

Fig. 4. Reduced firing rate and altered firing patterns in transgenic neocortical neurons compared to controls.

(A) Mean (+SEM) spontaneous firing rates calculated for extracellular single unit recordings during SWS were lower for neurons of 5mo transgenic mice than for controls, but were not different during QW. Ctrl 5mo: n = 23 neurons from 3 mice; Tg 5mo: n = 23 neurons from 3 mice. **(B)** Mean (+SEM) spontaneous firing rates, calculated for intracellular recordings over all subthreshold states (left) and solely over time spent in Up states (right), were lower for neurons in transgenic mice than for controls. Ctrl 3mo: n = 18 neurons from 11 mice; Ctrl 5mo: n = 20 neurons from 11 mice; Tg 3mo: n = 11 neurons from 7 mice; Tg 5mo: n = 11 neurons from 8 mice. **(C)** Distribution histogram of mean (±SEM) within Up state ISIs and the mean (+SEM) value of within Up states ISIs per each group (inset) revealed neurons of 5mo transgenic mice had longer ISIs than controls. Histogram is presented in semi-log scale. Ctrl 3mo: n = 16 neurons from 11 mice; Ctrl 5mo: n = 19 neurons from 10 mice; Tg 3mo: n = 10 neurons from 6 mice; Tg 5mo: n = 10 neurons from 7 mice. **(D)** Distribution histogram of mean (±SEM) latency to first spike from Up transition point and mean (+SEM) value of latency to first spike from Up transition point per each group (inset) revealed neurons of transgenic mice had longer latencies than controls. Histogram is presented in semi-log scale. Ctrl 3mo: n = 15 neurons from 11 mice; Ctrl 5mo: n = 18 neurons from 10 mice; Tg 3mo: n = 9 neurons from 6 mice; Tg 5mo: n = 8 neurons from 8 mice. * $p < 0.05$. See also Table S2.

Figure 1

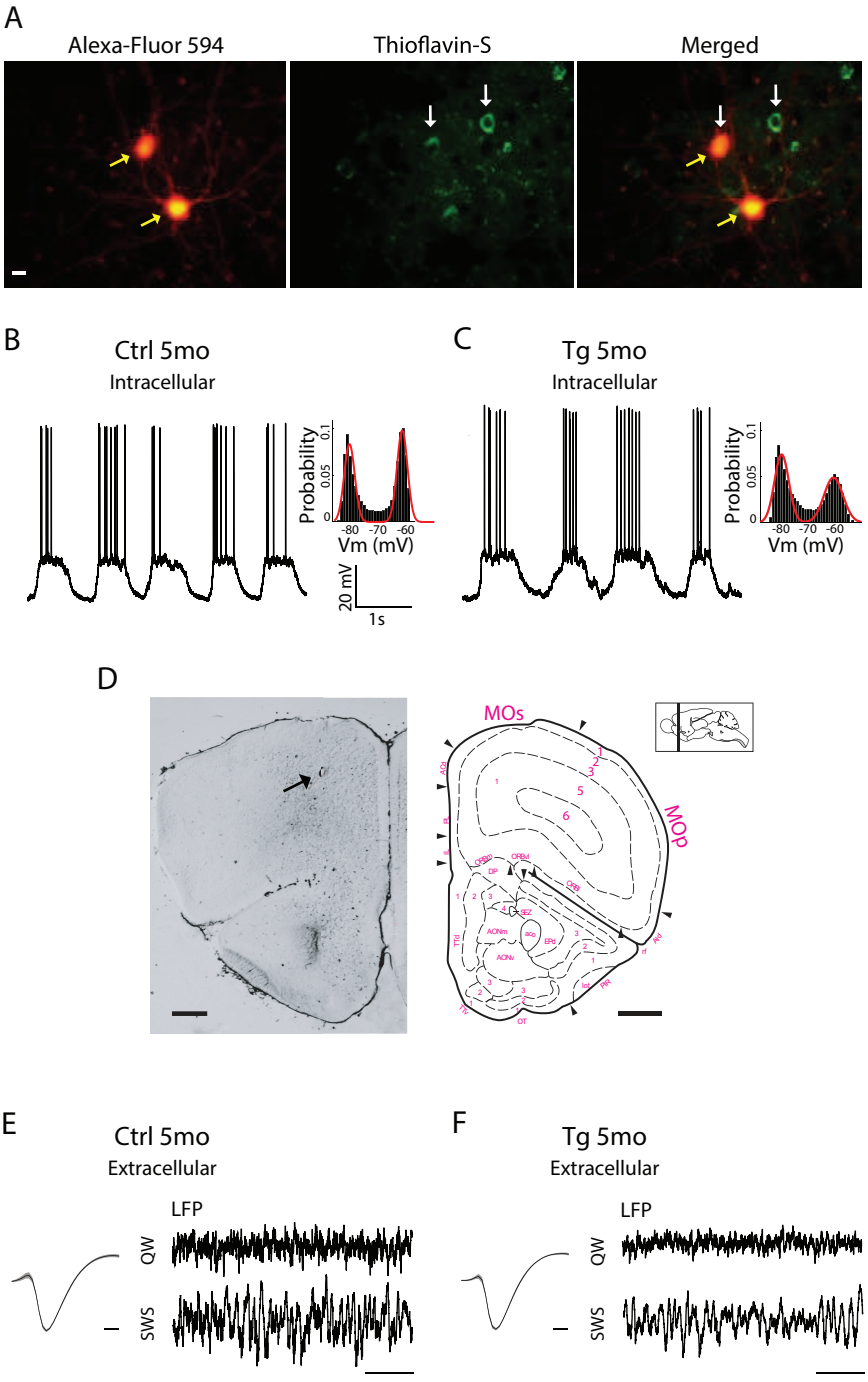
A
Alexa-Fluor 594
Thioflavin-S
Merged
B
Ctrl 5mo
Intracellular
Probability
Vm (mV)
20 mV
1s
C
Tg 5mo
Intracellular
Probability
Vm (mV)
D
MOs
MOP
E
Ctrl 5mo
Extracellular
LFP
QW
SWS
F
Tg 5mo
Extracellular
LFP
QW
SWS

Figure 2

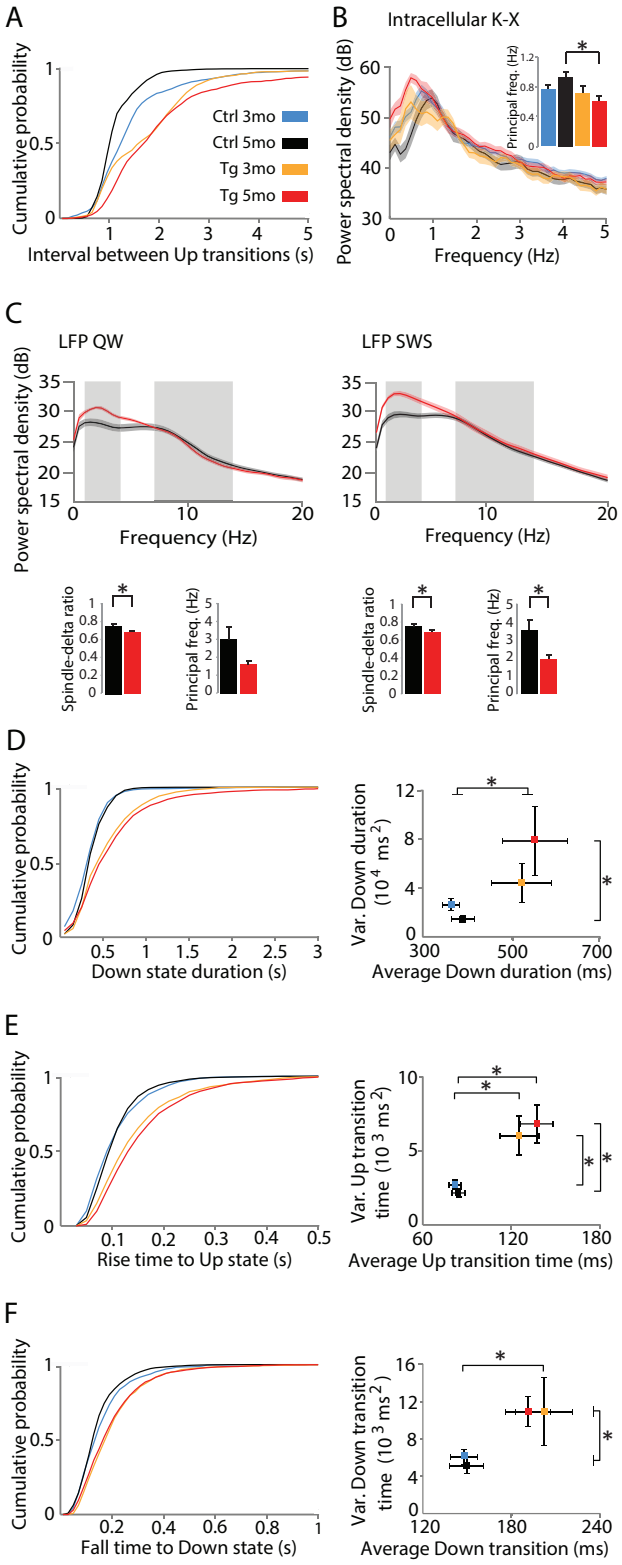
A
Cumulative probability
Interval between Up transitions (s)
Ctrl 3mo
Ctrl 5mo
Tg 3mo
Tg 5mo
B
Intracellular K-X
Power spectral density (dB)
Frequency (Hz)
Principal freq. (Hz)
C
LFP QW
LFP SWS
Power spectral density (dB)
Frequency (Hz)
Spindle-delta ratio
Principal freq. (Hz)
D
Cumulative probability
Down state duration (s)
Var. Down duration (10^4 ms^2)
Average Down duration (ms)
E
Cumulative probability
Rise time to Up state (s)
Var. Up transition time (10^3 ms^2)
Average Up transition time (ms)
F
Cumulative probability
Fall time to Down state (s)
Var. Down transition time (10^3 ms^2)
Average Down transition (ms)

Figure 3

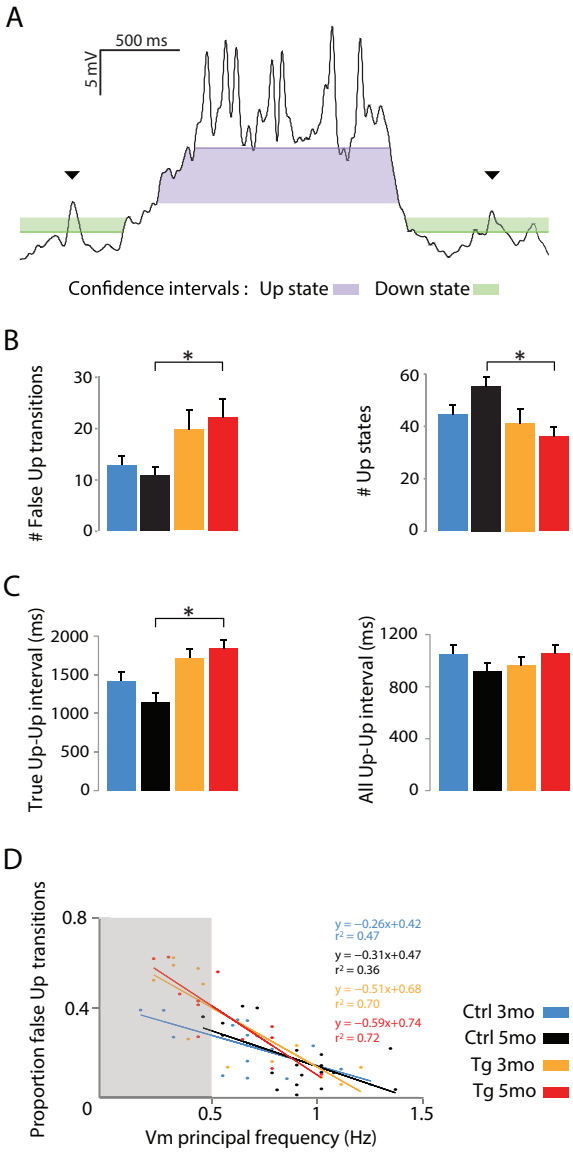
A
500 ms
5 mV
Confidence intervals : Up state Down state
B
False Up transitions
Up states
C
True Up-Up interval (ms)
All Up-Up interval (ms)
D
Proportion false Up transitions
Vm principal frequency (Hz)
y = −0.26x+0.42
r² = 0.47
y = −0.31x+0.47
r² = 0.36
y = −0.51x+0.68
r² = 0.70
y = −0.59x+0.74
r² = 0.72
Ctrl 3mo
Ctrl 5mo
Tg 3mo
Tg 5mo

Figure 4

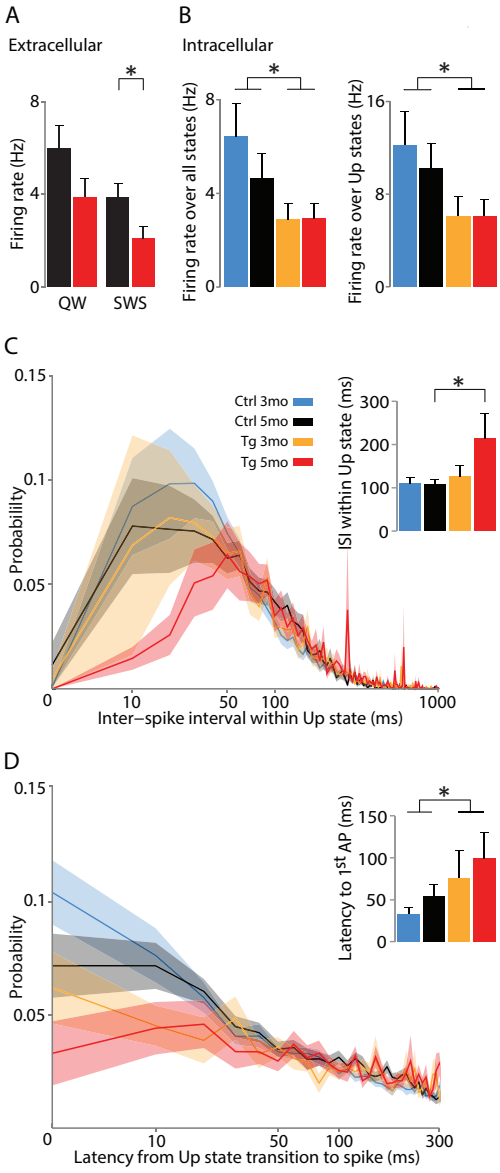
A
Extracellular
Firing rate (Hz)
8
4
0
QW
SWS
*
B
Intracellular
Firing rate over all states (Hz)
Firing rate over Up states (Hz)
16
C
Ctrl 3mo
Ctrl 5mo
Tg 3mo
Tg 5mo
Probability
0.15
0.1
0.05
0
10
50
100
1000
Inter–spike interval within Up state (ms)
ISI within Up state (ms)
300
200
100
D
Latency to 1st AP (ms)
150
50
300
Latency from Up state transition to spike (ms)

SUPPLEMENTAL INFORMATION

Menkes-Caspi et al.: Pathological tau disrupts ongoing network activity

Supplemental data

Figure S1 and S2, related to main figure 1.

Tables S1 and S2, related to main figures 1 and 4, respectively

Supplemental experimental procedures

Supplemental references

Related to supplemental experimental procedures

SUPPLEMENTAL DATA

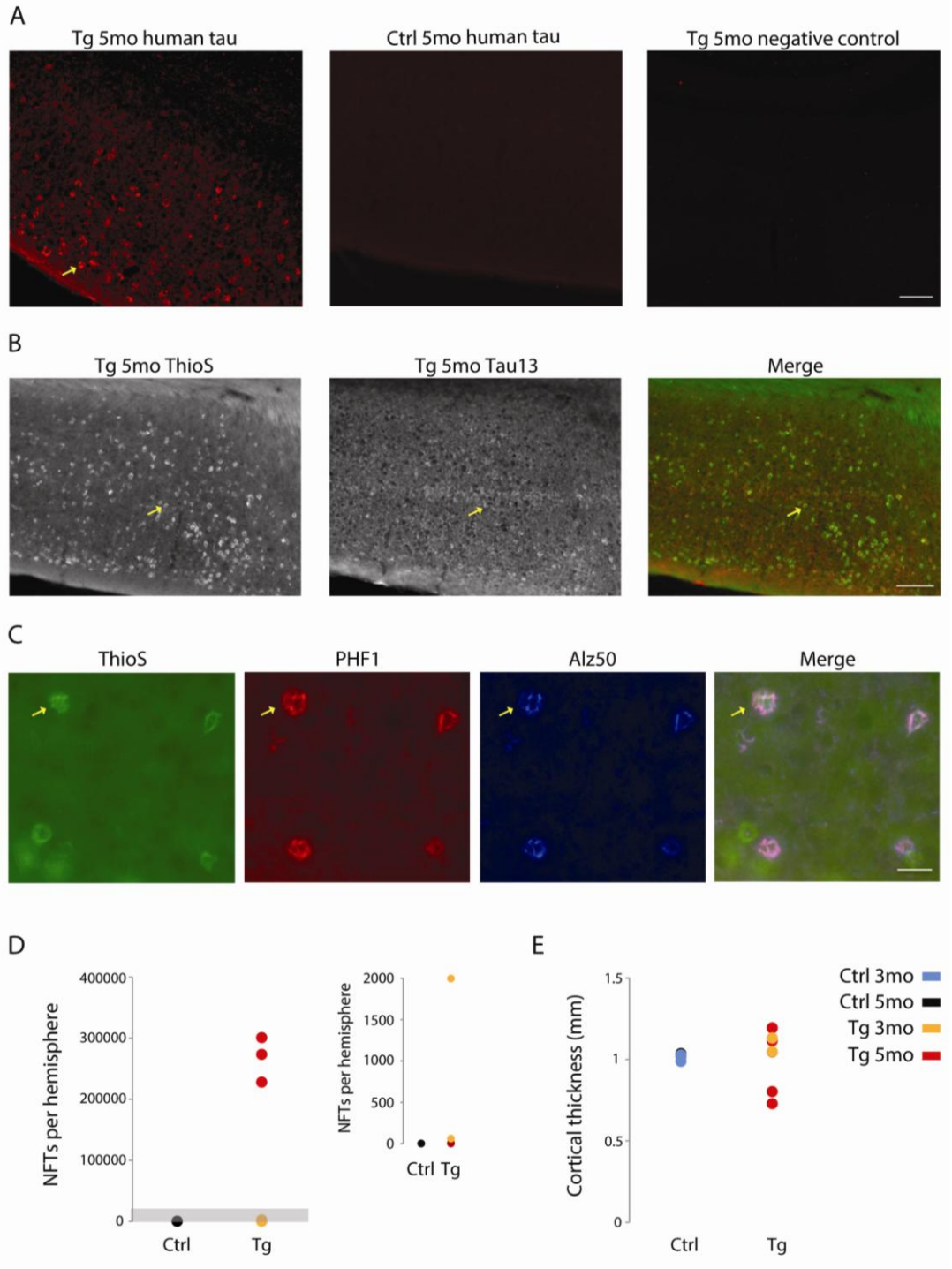

Supplemental Figure S1, related to Figure 1: **Pathological quantification of rTg4510 brains.**

(A) Human tau is expressed in the neocortex of rTg4510 transgenic mice. Human tau protein staining (Tau13) was exhibited by a 5mo transgenic mouse (left), but not by a 5mo control mouse (center) or a 5mo transgenic lacking the primary antibody, which served as a negative control (right). Yellow arrow indicates cell positive for Tau13. Scale bar, 100 µm. **(B)** Mature NFTs accumulate in the neocortex of 5mo transgenic mice, as seen by ThioS staining (left). Human tau is also expressed, as displayed by Tau13 staining (center). Merged image shows mature NFTs consist of human tau (right). Yellow arrows indicates cell positive for Tau13 and/or ThioS. Scale bar, 100 µm. **(C)** rTg4510 transgenic mice have accumulations of mature ThioS positive NFTs (left) and exhibit hyperphosphorylated (PHF1, center left) and misfolded tau (Alz50, center right) in the neocortex. Merged image shows NFTs to be aggregates of hyperphosphorylated misfolded tau (right). Yellow arrow indicates cell positive for ThioS, PHF1 and Alz50. Scale bar, 25 µm. **(D)** Transgenic mice from 3mo and 5mo age cohorts exhibited significant NFT aggregation (right), while control mice did not display any pathology (left). Inset plot shows an enlarged version of the lower part of the histogram (shaded), revealing low NFT counts for 3mo transgenic mice and for some 5mo transgenic mice and no pathology in either control groups. Transgenic mice from the 5mo cohort had variable yet significantly higher levels of NFT accumulation than 3mo transgenic mice ($p = 0.02$, t-test). Circles represent average value per mouse. **(E)** Cortical thickness in transgenic mice (right) from 3mo and 5mo age cohorts was not altered in comparison to control mice (left; $p = 0.83$, t-test), also when tested only for 5mo transgenic mice compared to age-matched controls ($p = 0.6$, t-test). Circles represent average value per mouse. Ctrl 3mo: n = 2 mice; Ctrl 5mo: n =

4 mice; Tg 3mo: n = 2 mice; Tg 5mo: n = 6 mice. Groups were compared by a two-tailed student's t-test.

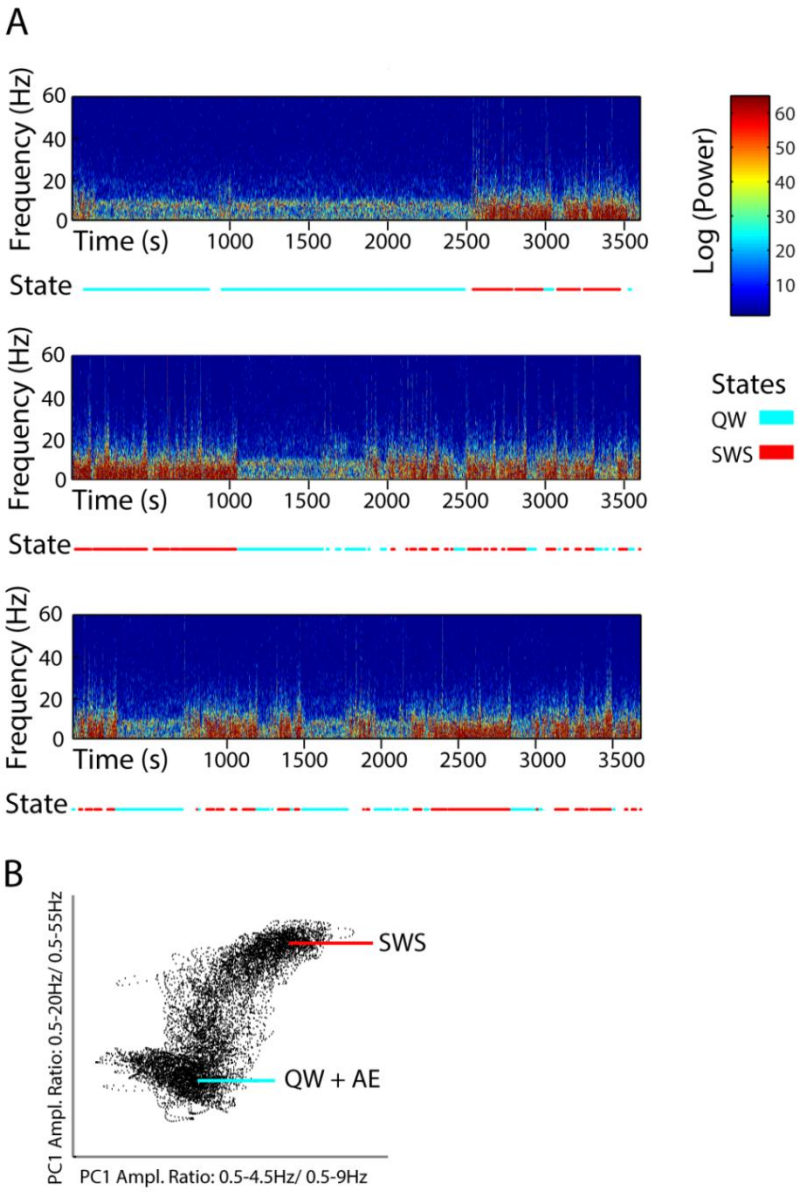

Supplemental Figure S2, related to Figure 1: **Verification of SWS and QW epochs in extracellular data.**

(A) Example of three consecutive LFP power spectrograms (top image of each top, center and bottom sections), each spanning 1 hour of recording, from a single 3-hour recording session from the cortex of a 5mo transgenic mouse. Spectrograms are aligned with the color-coded temporal sequence of QW and SWS states (bottom image of each top, center and bottom sections), assessed by the 2D state map (B) and cross validated by the experimenters' visual observation of the behavior of the mouse.

(B) Example of a two-dimensional state space for the same 5mo transgenic mouse as in (A), constructed for verification of visually encoded SWS and QW time epochs, as described in (Gervasoni et al., 2004). State space was defined by two spectral amplitude ratios calculated by dividing integrated spectral amplitudes at selected frequency bands from the above LFPs simultaneously recorded from different electrodes. Each point in the scatterplot represents 1 second of ongoing brain activity. In the example, the SWS cluster is located on the upper right quadrant of the state space, and the waking cluster, including active exploration (AE) and QW, occupies the lower right quadrant. State maps were well preserved across mice.

	Ctrl 3mo	**Ctrl 5mo**	**Tg 3mo**	**Tg 5mo**
Vm Up state Mean (mV)	-57.91 ± 4.45 (17)	-57.39 ± 5.99 (19)	-60.59 ± 5.09 (13)	-56.67 ± 6.23 (11)
Vm Up state Var. (mV^2)	11.51 ± 3.61 (17)	8.62 ± 3.76 (19)	11.51 ± 6.99 (13)	12.98 ± 5.08 (11)
Vm Down state Mean (mV)	-74.38 ± 7.51 (17)	-74.12 ± 6.67 (19)	-78.34 ± 6.93 (13)	-72.40 ± 5.53 (11)
Vm Down state Var. (mV^2)*	2.10 ± 1.07 (17)	1.76 ± 1.46 (19)	3.57 ± 3.56 (13)	2.76 ± 1.78 (11)
ΔVm (mV)	16.47 ± 4.47 (17)	16.73 ± 4.57 (19)	17.75 ± 3.85 (13)	15.72 ± 3.77 (11)
R_{in} Down state (MΩ)	32.21 ± 22.11 (7)	45.85 ± 23.78 (6)	39.58 ± 13.91 (7)	56.91 ± 10.46 (5)
R_{in} Up state (MΩ)	40.42 ± 33.55 (7)	31.23 ± 24.26 (6)	36.05 ± 16.19 (7)	61.2 ± 38.67 (5)
τ (ms)	4.23 ± 2.97 (7)	5.58 ± 3.73 (8)	3 ± 1.03 (7)	6.3 ± 3.81 (5)

Supplemental Table S1, related to Figure 1: **Passive electrophysiological properties of intracellularly recorded neocortical pyramidal neurons.**

All values are displayed as mean ± SD between cells (in parentheses are number of cells) over averaged values for each neuron in the group.

V_m values represent membrane potential values (in millivolts) within Up and Down states. Var. values represent within-variance of membrane potential (in mV^2) within Up and Down states. ΔV_m displays the difference between the mean values of the Up and Down states. R_{in} represents input resistance values (in megaohms) and τ represents membrane time constant values (in milliseconds).

Statistical analysis was performed using a Genotype × Age ANOVA with Tukey post-hoc tests. Asterisk denotes significance of variance of Down state Vm:

$p_{genotype} = 0.0284$ (genotype effect).

	Ctrl 3mo	Ctrl 5mo	Tg 3mo	Tg 5mo
AP threshold (mV)	-51.37 ± 4.61 (14)	-52.06 ± 4.84 (16)	-52.6 ± 3.38 (9)	-47.96 ± 6.43 (9)
AP amplitude (mV)*	63.79 ± 7.28 (14)	66.40 ± 8.96 (16)	61.50 ± 7.76 (9)	69.66 ± 8.79 (9)
AP half width (ms)	1.10 ± 0.18 (14)	1.05 ± 0.27 (16)	1.14 ± 0.18 (9)	1.09 ± 0.14 (9)
ΔV_m trajectory to spike (mV)	4.93 ± 2.16 (14)	5.07 ± 2.08 (16)	5.57 ± 2.01 (9)	6.04 ± 1.44 (9)

Supplemental Table S2, related to Figure 4: Firing properties of intracellularly recorded neocortical pyramidal neurons.

All values are displayed as mean ± SD between cells (in parentheses are number of cells) over averaged values for each neuron in the group.

AP threshold represents the threshold membrane potential (in millivolts) from which spikes arise. AP amplitude displays the voltage difference (in millivolts) between the peak of the spike and the spike threshold. AP half width displays the duration (in milliseconds) of the spike at half its amplitude. ΔV_m trajectory to spike represents the difference (in millivolts) between the spike threshold value and the membrane potential at 10 ms prior to spike threshold.

Statistical analysis was performed using a Genotype × Age ANOVA with Tukey post-hoc tests. Asterisk denotes significance of mean AP amplitude: $p_{age} = 0.0341$ (age effect).

SUPPLEMENTAL EXPERIMENTAL PROCEDURES

Tau pathology quantification

rTg4510 mice (Ctrl 3mo: n = 2; Ctrl 5mo: n = 4; Tg 3mo: n = 2; Tg 5mo: n = 6) were transcardially perfused and their brains removed. Brains were postfixed for at least 24 hours in 4% paraformaldehyde, and then cryoprotected in 30% sucrose solution for 48 hours. Brain hemispheres were cut into 50 µm coronal sections using a sliding microtome (SM2010R, Leica Microsystems, Milton Keynes, UK). Immunohistochemistry for tau was conducted as described previously (Pooler et al., 2013). Briefly, a series of every 10^{th} section (500 µm apart) through the hemisphere was stained with an antibody that recognized human tau (Tau13, MMS-520R, 1:500; Covance, Emeryville, CA), secondary donkey anti-mouse IgG conjugated to Alexa Fluor 594 (Life Technologies, Carlsbad, CA) and counterstained with 0.05% Thioflavin S (ThioS; Sigma-Aldrich) in 50% ethanol to label neurofibrillary tangles (NFTs). Another series of every 10^{th} section was stained with PHF1 (generous gift from Dr. Peter Davies, 1:1000) to label tau phosphorylated at serine 396 and 404, and with Alz50 (P. Davies, 1:500) to label misfolded tau. Secondary donkey anti-mouse IgG conjugated to Alexa Fluor 594 (Life Technologies) and goat anti-mouse IgM conjugated to Cy5 (Millipore, Billerica, MA) were used for detection. Sections were also stained with Thioflavin S as above to label mature NFTs.

To assess the number of NFTs per hemisphere, every 10^{th} section was examined for each mouse with an upright Zeiss Axioimager Z2 microscope with a Coolsnap HQ2 camera (Carl Zeiss Ltd, Cambridge UK) equipped with StereoInvestigator stereology software (MicroBrightField Europe e.K.). Stereological estimation of the number of NFTs per hemisphere was carried out as described previously (Spires et al., 2006) with minor modifications. Cortical thickness was measured at three equally

spaced points on every 10th section and averaged to estimate the cortical thickness for each animal. The amount of pathology between transgenic mice was variable, thus necessitating two tangle counting schemes. For animals with very few tangles, all tangles present in the cortex on every 10th section were counted. This number was multiplied by 10 to estimate the total number of tangles per hemisphere. For animals with more substantial pathology (precluding counts of all tangles on every 10th section), the optical disector method was used. Briefly, the neocortex was outlined on every 10th section through the hemisphere, and the area of those regions was multiplied by 10 and summed to estimate the total cortical volume. A 100 × 100 micron sampling probe (disector) was placed in a randomly oriented grid every 300 micrometers throughout the neocortex on every 10th section. All ThioS positive neurons were counted in the disector (excluding those that touched the left and bottom edge of the disector). The number of ThioS positive neurons counted per mouse was divided by the total volume of disectors (100 microns × 100 microns × 50 microns thick × number of sample sites) to calculate a density of NFTs per cortical volume. This density of NFTs was multiplied by the estimated total cortical volume to give an estimate of the total number of NFTs per hemisphere.

SUPPLEMENTAL REFERENCES

Pooler, A.M., Polydoro, M., Wegmann, S.K., Pitstick, R., Kay, K.R., Sanchez, L., Carlson, G.A., Gomez-Isla, T., Albers, M.W., Spires-Jones, T.L., and Hyman, B.T. (2013). Tau-amyloid interactions in the rTgTauEC model of early Alzheimer's disease suggest amyloid-induced disruption of axonal projections and exacerbated axonal pathology. The Journal of Comparative Neurology 521, 4236-4248.